Modelling Simul. Mater. Sci. Eng. **19** (2011) 085008 (14pp) doi:10.1088/0965-0393/19/8/085008

Interatomic potential to study plasticity in stainless steels: the FeNiCr model alloy

G Bonny[1], D Terentyev[1], R C Pasianot[2,3,4], S Poncé[1,5] and A Bakaev[1,6]

[1] SCK·CEN, Nuclear Materials Science Institute, Boeretang 200, B-2400 Mol, Belgium
[2] CAC-CNEA, Departamento de Materiales, Avda. Gral. Paz 1499, 1650 San Martín, Pcia. Buenos Aires, Argentina
[3] CONICET, Avda. Rivadavia 1917, 1033 Buenos Aires, Argentina
[4] UNSAM/CNEA, Instituto Sabato, Avda. Gral. Paz 1499, 1650 San Martín, Pcia. Buenos Aires, Argentina
[5] Université Catholique de Louvain, Institute of Condensed Matter and Nanosciences, Chemin du cyclotron 2 bte L7.01.07, B-1348 Louvain-la-Neuve, Belgium
[6] Ghent University, Center for Molecular Modeling, Technologiepark 903, B-9052 Zwijnaarde, Belgium

E-mail: gbonny@sckcen.be

Received 15 May 2011, in final form 7 September 2011
Published 3 November 2011
Online at stacks.iop.org/MSMSE/19/085008

Abstract

Austenitic stainless steels are commonly used materials for in-core components of nuclear light water reactors. In service, such components are exposed to harsh conditions: intense neutron irradiation, mechanical and thermal stresses, and aggressive corrosion environment which all contribute to the components' degradation. For a better understanding of the prevailing mechanisms responsible for the materials degradation, large-scale atomistic simulations are desirable. In this framework we developed an embedded atom method type interatomic potential for the ternary FeNiCr system to model movement of dislocations and their interaction with radiation defects. Special attention has been drawn to the Fe–10Ni–20Cr alloy, whose properties were ensured to be close to those of 316L austenitic stainless steel. In particular, the stacking fault energy and elastic constants are well reproduced. The fcc phase for the Fe–10Ni–20Cr random alloy was proven to be stable in the temperature range 0–900 K and under shear strain up to 5%. For the same alloy the stable glide of screw dislocations and stability of Frank loops was confirmed.

(Some figures may appear in colour only in the online journal)

1. Introduction

Austenitic stainless steels are commonly used materials for in-core components of nuclear light water reactors (LWRs) [1, 2]. In service, such components are exposed to harsh conditions:

intense neutron irradiation, mechanical and thermal stresses and aggressive corrosion environment. This combination of factors allows the occurrence of irradiation assisted stress corrosion cracking (IASCC), radiation induced creep and swelling, which all limit life time of the in-core components. So far, the available knowledge on degradation of the internal components of LWRs originates mainly from either the analysis of materials extracted from power reactor components, or tests on materials irradiated in test reactors or using accelerator facilities. In order to optimize in-service lifetime and avoid costly replacement campaigns, a deeper fundamental understanding of the above-mentioned degradation mechanisms is desirable, which hopefully could serve as input for engineering- and design-level modelling.

In this framework two work packages within the European project PERFORM60 are dedicated to study the micro-structure and plasticity laws of 316L stainless steels [3]. In this project multi-scale modelling techniques and experiments on FeNiCr model alloys are combined to gain a deeper understanding of the prevalent degradation mechanisms. As a part of the multi-scale modelling effort, atomistic simulations are foreseen to investigate the effects of radiation damage on the alloy's micro-structure and dislocation mobility. For this, ternary FeNiCr interatomic potentials, which can mimic mechanical properties of 316L stainless steels, must be developed. At the same time, the potential should acquire a relatively simple formalism, which allows for million-atom simulations within a reasonable computational time. Hence, the embedded atom method (EAM) [4] formalism was taken as a natural choice. Since the requirements with respect to micro-structure and plasticity are essentially different and not necessarily compatible within a single interatomic potential framework, two sets of potentials will be developed.

Here we focus on the requirements regarding plasticity studies at atomic level. For this purpose the essential materials properties to be fitted in a large concentration range near the target composition of 316L steel (i.e. Fe–10Ni–20Cr), are three, namely, stability of the fcc phase, elastic constants and stable stacking fault energy (SFE). In addition, the potential must provide the stability of the fcc phase under large deformation (up to 5% shear strain), stability of Frank loops (of size at least up to 10 nm) and ensure stable dislocation glide in a wide temperature (0–900 K) and composition range (5–30% Ni and Cr).

In the literature two different EAM FeNiCr (N and H) potentials were developed by Grujicic and Zhou [5] and Smith and Was [6], respectively. However, in these latter works the full parametrization of the potential is not reported. With respect to available potentials for binary alloys, no advantage could be taken either of state-of-the-art FeNi [7, 8] nor FeCr [9, 10] potentials. Namely, at the target composition of 10% Ni and 20% Cr with the latter potentials, it was tested that at finite temperature and under strain the fcc phase is not (meta)stable and a spontaneous transformation to the bcc phase occurs. An alternative for the Fe part of the potentials described in [7–10] could be the bond order potential developed in [11] that reproduces the experimentally observed bcc–fcc–bcc transition with temperature. However, such an approach does not necessarily guarantee fcc stability in the concentration range of interest as in 316L steels both carbon and nitrogen play an important role in stabilizing the fcc phase, which is not considered in the present simplified model alloy. Therefore a new FeNiCr ternary potential is fitted including the pure elements.

2. Methods

2.1. Energy model

The atomic interactions are described using the EAM [4], which is widely used to describe metals and their alloys. In addition to pair interactions, V, this approach includes an embedding

energy, F, dependent on the local electron density, ρ. The latter term approximates the many-body contribution of all nearby atoms. The total energy within EAM is given as

$$E = \frac{1}{2} \sum_{\substack{i,\, j\,=\,1 \\ j \neq i}}^{N} V_{t_i t_j}(r_{ij}) + \sum_{i=1}^{N} F_{t_i}(\rho_i). \tag{1}$$

Here N represents the total number of atoms in the system, r_{ij} is the distance between atoms i and j and t_i denotes chemical species (Fe, Ni or Cr in our case). The local electron density around atom i, contributed from its neighbours is given as

$$\rho_i = \sum_{\substack{j\,=\,1 \\ j \neq i}}^{N} \phi_{t_j}(r_{ij}), \tag{2}$$

where ϕ denotes the electron density function of the considered element. Thus, for the FeNiCr ternary system twelve functions need to be defined: ϕ_{Fe}, ϕ_{Ni}, ϕ_{Cr}, F_{Fe}, F_{Ni}, F_{Cr}, V_{FeFe}, V_{NiNi}, V_{CrCr}, V_{FeNi}, V_{FeCr} and V_{NiCr}.

In this work, the electron density function ϕ is defined as the product of a Thomas–Fermi screening function and a cut-off,

$$\phi(r) = S \frac{\exp(-\beta r)}{r} \frac{x^4}{1 + x^4}. \tag{3}$$

Here S is a normalization factor, $x = (r - r_{\mathrm{cut}})/h$, with β and h fitting parameters and r_{cut} the cut-off distance. The pair potential V is defined as a linear combination of piecewise cubic splines and the electron density function ϕ,

$$V_{XY}(r) = \sum_{k=1}^{N_p} [a_k (r_k - r)^3 \Theta(r_k - r)] - K \phi_Y(r) \delta_{XY}. \tag{4}$$

Here r_k are the knots, a_k fitting parameters, Θ the Heaviside unit step function and δ Kronecker's delta. The dependence on ϕ stems from the effective gauge transformation [12–15] on the pure potentials from which K is derived. The embedding function F is parametrized as

$$F = A\sqrt{\rho} + B\rho + C\rho^2 + D\rho^4, \tag{5}$$

with A, C and D fitting parameters. The linear term in ρ follows from the same effective gauge transformation from which B is derived. The optimized parameter set for the present potential is given in the appendix.

2.2. Fitting strategy

Prior to the cross interactions, the potentials for the pure elements were fitted. The material properties considered in these fits are the stability of different crystallographic structures (bcc, fcc, fct and hcp), their cohesive energy E_{coh}, and equilibrium lattice (with lattice constants a, b and c), the elastic constants for the equilibrium lattice (in our case cubic) C_{11}, C_{12}, C_{44} [16], vacancy formation and migration energy, formation energy of self-interstitial configurations ($\langle 1\,0\,0 \rangle$, $\langle 1\,1\,0 \rangle$ and $\langle 1\,1\,1 \rangle$ dumbbells, tetrahedral and octahedral sites), stable SFE and Rose's equation [17]. As a first approximation, these properties were expressed using a rigid lattice, so that the resulting formulae are linear in the fitting parameters $\{a_k, A, B, C, D\}$, for given β, h and r_{cut}. The former were optimized by a weighted least square fit to the target properties for each chosen set $\{\beta, h, r_{\mathrm{cut}}\}$. In this way, $\{\beta, h, r_{\mathrm{cut}}\}$ are manually tuned aiming at best

matching the relaxed properties to the target values for each trial potential. This strategy allowed for a satisfactory result in a reasonable number of iterations.

For the alloy, the SFE as a function of composition and the elastic constants for the Fe–10Ni–20Cr target composition were fitted. The latter fits were performed using a variance expansion of the energy for a random alloy [7]. This method allows one to write the energy (and its derivatives) as a linear combination of the fitting parameters $\{a_k\}$, which were optimized following a least square fit to the target values. The average energy per atom in a random alloy is given as

$$\begin{aligned}
\langle E_{\text{alloy}}\rangle &= \sum_X C_X \langle E_X\rangle,\\
\langle E_X\rangle &= \frac{1}{2}\sum_Y \sum_\nu N_\nu C_Y V_{XY}(r_\nu) + F_X(\langle\rho_X\rangle) + \frac{1}{2}\langle\sigma_X^2\rangle F_X''(\langle\rho_X\rangle),\\
\langle\rho_X\rangle &= \sum_Y \sum_\nu N_\nu C_Y \phi_Y(r_\nu),\\
\langle\sigma_X^2\rangle &= \sum_Y \sum_\nu N_\nu C_Y(1-C_Y)\phi_Y(r_\nu)^2 - \sum_{\substack{Y,\,Z\\ Y\neq Z}} \sum_\nu N_\nu C_Y C_Z \phi_Y(r_\nu)\phi_Z(r_\nu).
\end{aligned} \tag{6}$$

Here the sum over X (Y and Z) runs over all elements in the alloy while ν runs over the neighbour shells, with N_ν the number of atoms in shell ν and C_X the concentration of element X. This expression is derived in a similar way as in [7] by treating the random alloy as a multi-nomial distribution of solutes.

The expressions for the elastic constants, C_{ijkl}, are derived through the method of uniform deformations, where every atomic position, $\vec{r}$, is subject to the transformation, $\vec{r}' = (1-\bar{\bar{\varepsilon}})\vec{r}$, with $\bar{\bar{\varepsilon}}$ the small strain tensor. Thus, by evaluating the change in the above average energy per atom up to 2nd order in the components of the latter, one obtains (see e.g. [5])

$$C_{ijkl} = \frac{1}{\Omega}\frac{\partial^2\langle E_{\text{alloy}}\rangle}{\partial\varepsilon_{ij}\partial\varepsilon_{kl}}, \tag{7}$$

where Ω is the atomic volume. For a cubic crystal, only three of these coefficients remain independent, e.g., $C_{11} = C_{1111}$, $C_{12} = C_{1122}$ and $C_{44} = C_{1212}$.

3. Results

3.1. Pure potentials

The static properties of the pure potentials are summarized in table 1 and compared with the target values selected from DFT data or experiments. As mentioned in the introduction, the purpose of the ternary potential is to describe the elastic and plastic properties of 316L steel in a large concentration range near the target composition. Therefore, we focused primarily on the correct reproduction of the elastic constants, the SFE and stability of the fcc phase (artificially imposed in the case of Fe and Cr). As shown in table 1, the fcc structure for both Fe and Cr was artificially stabilized to avoid possible instabilities observed using bcc Fe and Cr potentials mentioned in the introduction. With respect to the target values, high weight was given only to Ni, since this element has the fcc lattice as a physical ground state. For Ni, the lattice parameter a, cohesive energy E_{coh} and the energy difference relative to other structures ΔE_0 are taken from experiment [18] and density functional theory (DFT) calculations [19]. For Fe and Cr the target values come from DFT calculations [8, 21, 20] and [22], respectively.

Table 1. Static properties of the pure elements. For the cases where two target values are reported we refer to the range. References for the target values are provided in the text.

	Iron		Nickel		Chromium	
	Target	Potential	Target	Potential	Target	Potential
E_{coh} (fcc) (eV/at.)	—	4.12	4.45	4.45	—	3.69
ΔE_{coh} (fcc-bcc) (eV/at.)	−0.16	+0.11	+0.15	+0.19	−0.39	+0.05
ΔE_{coh} (fcc-hcp) (eV/at.)	—	0.00	+0.03	+0.02	—	+0.04
a (fcc) (Å)	3.425[a]	3.499	3.519	3.519	3.610	3.584
a (hcp) (Å)	—	2.474[b]	—	2.488[c]	—	2.523[d]
a (bcc) (Å)	2.867	2.962[e]	2.801	2.801	2.878	3.149[f]
C_{11} (GPa)	141	141	247	247	249	247
C_{12} (GPa)	100	100	147	147	178	183
C_{44} (GPa)	108	108	125	125	143	145
E_{SF} (mJ m^{-2})	4	0	111–128	113	341	272
E_m (Vac) (eV)	0.95–1.05	0.61	1.08–1.30	1.17	2.19	2.25
E_f (Vac) (eV)	1.89–1.95	1.94	1.45–1.79	1.48	2.14	2.11
E_f ($\langle 1\,0\,0\rangle$ SIA) (eV)	3.53–3.65	3.60	4.07–4.11	4.08	—	5.10
E_f ($\langle 1\,1\,0\rangle$ SIA) (eV)	—	3.91	4.99–4.91	4.71	—	5.60
E_f ($\langle 1\,1\,1\rangle$ SIA) (eV)	4.56	4.61	4.69–4.72	4.76	—	5.40
E_f (Octa SIA) (eV)	4.35	3.87	4.25–4.32	4.89	—	5.71
E_f (Tetra SIA) (eV)	4.32	4.58	4.69–4.71	4.99	—	5.56

[a] $c/a = 1.065$.
[b] $c/a = 1.633$.
[c] $c/a = 1.663$.
[d] $c/a = 1.736$.
[e] $c/a = 0.895$.
[f] $c/a = 0.793$.

An excellent agreement with the target values is observed for Ni, while both Fe and Cr show poor agreement.

For Ni, the elastic constants are in excellent agreement with the experimental values [23]. Since both Fe and Cr are unstable in the fcc phase, no data for their elastic constants are available. The reported target values are therefore linear extrapolations of the experimentally measured elastic constants of Ni–Fe and Ni–Cr fcc solid solutions taken from [6, 23], thereby following the same strategy as Grujicic and Zhou [5]. As shown in table 1, the elastic constants resulting from both Fe and Cr potentials are in excellent agreement with the target values.

The target values for the stable fcc stacking fault are based on experiment (128 mJ m^{-2} for Ni) [24] and the extrapolation of low temperature (300 K) thermodynamic calculations (all other values) [25]. The latter calculations are polytope expansions [26] based on Calphad type free energy parametrizations for fcc and hcp phases. The latter have been shown to be in excellent agreement with experimental data for (Fe,Ni,Cr) solid solutions (see [25] and references therein). For both Fe and Ni potentials the SFE is in excellent agreement with the target values. For the Cr potential, however, the target value is underestimated by ∼70 mJ m^{-2}. Given the instability of fcc Cr, this outcome is, however, of minor importance, as long as the correct trend in the order of SFE for the alloy is reproduced (see below).

In figure 1 the $\langle 1\,1\,2\rangle$ $\{1\,1\,1\}$ gamma lines are presented for the pure potentials, from which the unstable stacking fault can be determined. The latter is connected to the mobility of 1/6 $\langle 1\,1\,2\rangle$ Shockley partial dislocations, for which a smooth gamma line is desirable, a characteristic that is reproduced by the potential.

The target vacancy migration and formation energy, reported in table 1 is obtained from DFT calculations and experimental data. In particular, for fcc Fe and Cr these are DFT data

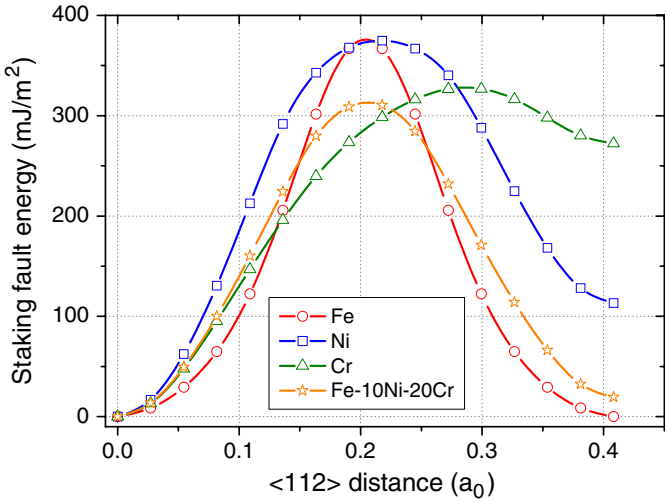

Figure 1. ⟨1 1 2⟩ {1 1 1} gamma cut calculated for the pure elements and Fe–10Ni–20Cr.

from [21, 22], while for fcc Ni we took experimental data from [18] and DFT data from [20]. It must be noted that relaxation of point defects in a fcc Cr matrix cannot be performed due to the instability of the phase and therefore only unrelaxed data are reported. As shown in table 1 the values obtained from the potential are in excellent agreement with the target ones, except for the vacancy migration barrier in Fe, which is largely underestimated. The energy reported for Cr correspond to non-relaxed structures for the sake of comparison with DFT.

The target formation energies of the different SIA configurations in Fe and Ni are obtained from DFT calculations [21–22]. No DFT data for SIAs in fcc Cr are available due to the above-mentioned phase instability. From table 1 it is clear that all potentials predict a ⟨1 0 0⟩ dumbbell to be the ground state, in agreement with the DFT results. The formation energy of a ⟨1 0 0⟩ dumbbell as well as its relative stability against other SIA configurations is in excellent agreement with DFT.

In figure 2 the average lattice energy, $E^* = E/E_{\mathrm{coh}}$, under uniform expansion and contraction (with strain $a^* = 9\Omega B/E_{\mathrm{coh}}(a/a_0 - 1)$, with B the bulk modulus) calculated with the different potentials is compared with Rose's universal equation of state [17]. Both Ni and Cr potentials reproduce well the equation of state. For Fe, there is poor agreement with Rose's equation for both large contraction and expansion. The former is due to the incompatibility with the ⟨1 0 0⟩ dumbbell formation energy while the latter is due to the short interaction range of the potential (4.0 Å compared with 5.6 Å for both Ni and Cr).

3.2. Alloy

3.2.1. Stacking fault energy. The stable SFE maps obtained from the potential and thermodynamic calculations [25] are compared in figure 3. For the potential the SFE was sampled with an interval of 10%. Each data point was obtained by averaging over 30 runs varying the distribution of solutes in the Fe matrix. The crystals containing in total 6000 atoms were fully relaxed. The resulting error on the average was at most 3.5 mJ m^{-2} (the error is defined as the 95% confidence interval around the average value; i.e. 1.96 times the standard error). Around the target composition, Fe–10Ni–20Cr, the thermodynamic calculations are reproduced as well as experimental results for 316L steels—23 mJ m^{-2} [25] and 10–30 mJ m^{-2}

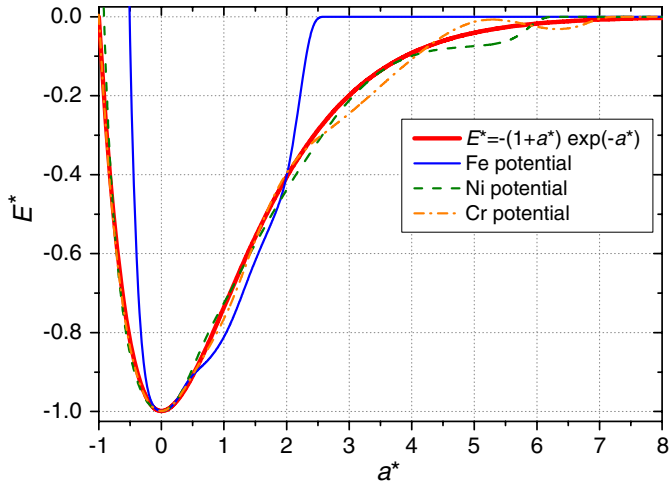

Figure 2. Evaluation of Rose's equation for the different potentials.

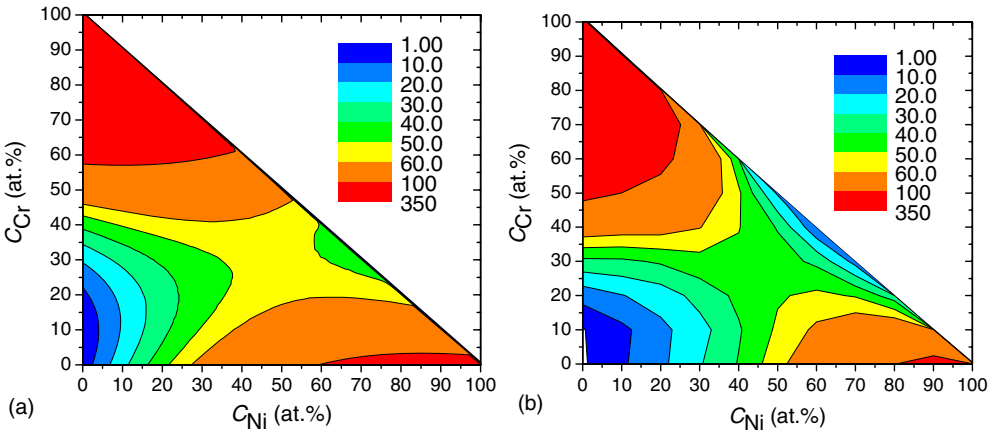

Figure 3. The stable SFE (mJ m^{-2}) as function of composition obtained from thermodynamic calculations [25] (*a*) and the potential (*b*).

[27–29] versus 20 mJ m^{-2} obtained with the potential. The potential also reproduces correct trends in SFE when varying Cr and Ni content. As a matter of fact, the saddle around Fe–45Ni–30Cr is reproduced.

Also worth of noticing is that the $\langle 1\,1\,2\rangle$ $\{1\,1\,1\}$ gamma line for the Fe–10Ni–20Cr alloy, superposed in figure 1, is smooth and exhibits a single hump, as in the case of the pure elements.

3.2.2. Elastic properties. In table 2 the elastic properties of our potential for the Fe–10Ni–20Cr alloy are compared with experimental values obtained in mono-crystals of 316L steels [30–32]. For the experimental data we also report the scattering range. C_{11}, C_{12} and C_{44} are the three independent elastic constants for cubic crystals), $B = (C_{11}+2C_{12})/3$ is the bulk modulus, $C' = (C_{11} - C_{12})/2$ is the tetragonal shear modulus, $G = (3C_{44} + 2C')/5$ is the isotropic shear modulus, $A = C_{44}/C'$ is the anisotropy ratio (dimensionless) and $y = C_{12}/C_{11}$ the relative constancy (dimensionless). The elastic constants for the random alloys were obtained

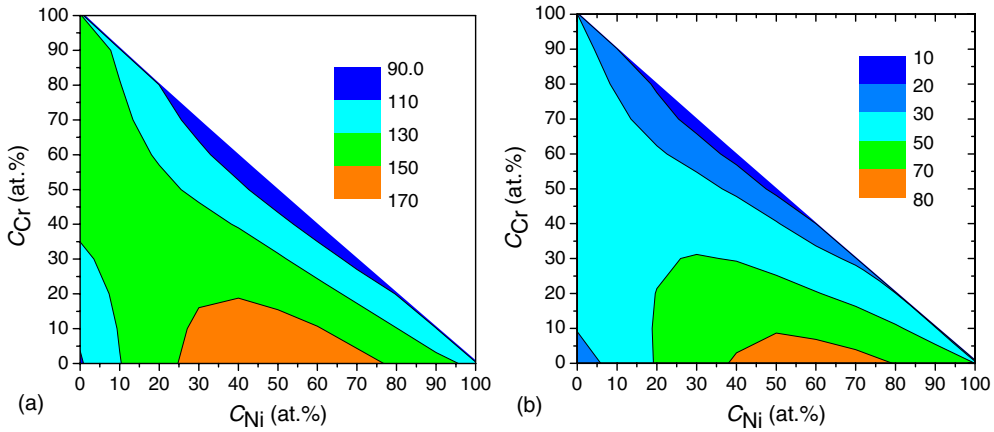

Figure 4. C_{44} (*a*) and C' (*b*) as a function of composition at 0 K.

Table 2. Comparison of the elastic constants (GPa) between the potential for the Fe–10Ni–20Cr alloy and 316L stainless steels [30–32].

	C_{11}	C_{12}	C_{44}	B	C'	G	A	y
Exp.	204–226	132–134	111–122	157–164	35–46	81–92	2.4–3.5	0.59–0.66
Pot.	214	136	129	162	39	93	3.3	0.64

by the deformation and subsequent relaxation of cubic boxes containing 2048 atoms. The resulting error on the average was less than 1 GPa. Clearly, the obtained values are in excellent agreement ($<10\%$) with the experimental data.

In figure 4 both C_{44} and C' are plotted in the whole composition range. The latter constants define the upper and lower bounds, respectively, for the shear modulus. For our purpose, C' is of particular interest since it defines the stability of the fcc phase with respect to small deformation. For the fcc phase to remain stable under deformations, C' must be strictly larger than zero (in practice $>\sim$10 GPa). As shown in figure 4(*b*), C' exceeds 10 GPa in the whole concentration range and is above 30 GPa for the target composition.

Figure 5 presents the shear modulus obtained by applying a pure shear of $\langle 1\,1\,0\rangle\{\text{-}1\,1\,1\}$ type to crystals containing about 40×10^3 atoms. This is the same type of shear as encountered by dislocations. The modulii were calculated as follows. Perfect crystals with different compositions (Fe–10Ni–20Cr, Fe–15Ni, Fe–15Cr, Fe–5Ni–10Cr and Fe–20Ni–40Cr) were thermalized and subsequently loaded by applying a shear strain at a constant rate of $10^7\ \text{s}^{-1}$. The loading was performed until the strain reached 5%. The simulation temperature was varied from 0 K up to 900 K. In all cases, the crystals kept fcc structure up to the maximum strain and no structural defects (e.g. faults) were found. The latter observation is consistent with figure 4 and confirms the stability of the fcc phase even under large deformation. In figure 5 the temperature effect on the shear modulus is illustrated by the vertical bar attached to the point corresponding to Fe–10Ni–20Cr alloy. Clearly, the effect of temperature is much weaker than the change in SFE due to the variation of composition.

3.2.3. Plastic properties As a validation of the developed potential for the modelling of dislocations we present some results obtained in Fe–10Ni–20Cr, Fe–15Ni and Fe–15Cr random

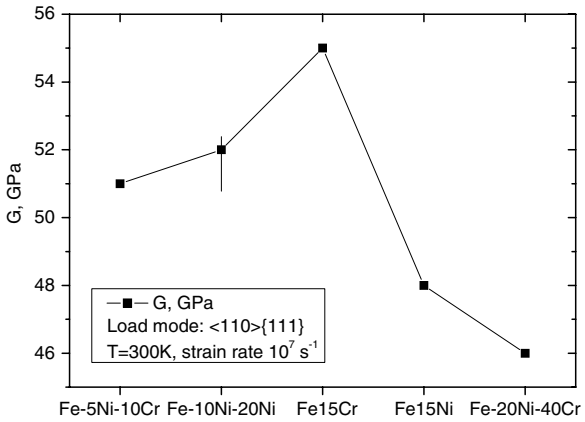

Figure 5. Shear modulus versus composition, measured at 300 K. The vertical bar attached to the point corresponding to Fe–10Ni–20Cr shows the variation of the shear modulus in the temperature range 0–900 K.

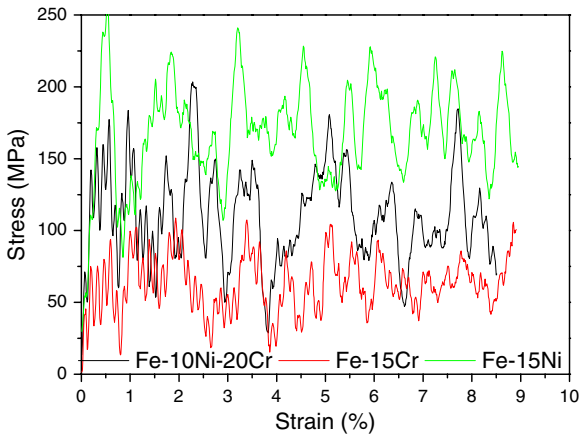

Figure 6. Evolution of the resolved shear stress in Fe–10Ni–20Cr, Fe–15Ni and Fe–15Cr crystals containing a $1/2\langle 1\,1\,0\rangle\{1\,1\,1\}$ screw dislocation. Simulation temperature is 300 K.

alloys. The crystals containing a $1/2\langle 1\,1\,0\rangle\{1\,1\,1\}$ screw dislocation were first relaxed, then thermalized at 300 K and finally loaded, by applying a pure shear at constant strain rate of $10^8\ \mathrm{s}^{-1}$. To study the dislocation movement we have applied a model of a periodic array of dislocations developed by Osetsky and Bacon [33]. In this model, the principal axes of the simulation crystal are oriented along the $x = \langle 1\,1\,0\rangle$, $y = \langle 1\,1\,2\rangle$ and $z = \langle 1\,1\,1\rangle$ directions and periodic boundaries are applied along the x- and y-axes, whereas atoms are fixed in the few upper and lower planes normal to the z direction. Shear strain is applied by displacement of the upper block of fixed atoms at constant velocity. The crystal contains about 400k atoms and the corresponding dislocation density and velocity are $0.5 \times 10^{14}\ \mathrm{m}^2$ and $45\ \mathrm{m\,s}^{-1}$, respectively. The evolution of the resolved shear stress is presented in figure 6. In all the alloys the dislocation was split into two partials with a width of stacking fault ribbon of about 10 nm. The two partial dislocations were seen to execute uniform movement independent of each other. As a consequence, the width of the stacking fault ribbon was seen to vary between 7 and 12 nm. During the simulations no significant curvature on the lines of the partials was observed,

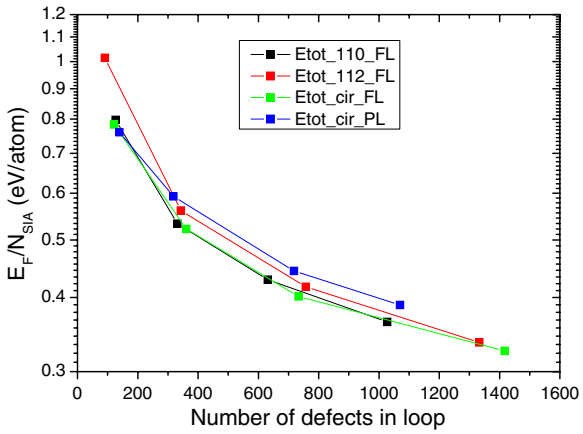

Figure 7. The formation energy of interstitial dislocation loops of different kinds calculated in the Fe–10Ni–20Cr alloy. See text for the explanation of the legend.

irrespective of the alloy composition. The friction stress, however, varies with composition; as follows from figure 6, increasing Ni or Cr content raises the friction stress. It is worth mentioning that the current simulations were performed at a relatively large strain rate—as proper behaviour at high rates ensures the same at lower strain rates—hence we expect that the friction stress will drop significantly when applying typical MD strain rates, i.e., 10^6–10^7 s^{-1}.

3.2.4. Dislocation loops Stability of Frank loops experimentally observed in irradiated austenitic steels is an important aspect with regard to the study of their impact on the pinning of dislocations. Using our potential, four different kinds of interstitial loops have been studied at 0 and 900 K. These are Frank loops of hexagonal shape with sides oriented along the ⟨1 1 0⟩ directions (henceforth 1 1 0_FL) and ⟨1 1 2⟩ directions (henceforth 1 1 2_FL), Frank loops of circular shape (henceforth cir_FL) and perfect loops of circular shape (henceforth cir_PL). The loop diameter was varied from 2 up to 10 nm.

The formation energy normalized by the number of interstitials forming the loop is presented in figure 7. We observe that for all studied sizes the perfect loops have a higher formation energy than any type of Frank loop. The latter observation is consistent with the low SFE reproduced by the potential and the experimental observation of Frank loops in 316L steels [34–36].

Having established that Frank loops are energetically most favourable, we have checked their stability against applied shear stress, as they may unfault under the action of stress of an approaching dislocation. We have observed the latter transformation in pure fcc crystals for relatively large loops [37] (whose self-energy is close to becoming higher than that of a perfect loop).

Relaxed Frank loops of size 10 nm were exposed to a ⟨1 1 0⟩{1 1 1} load by applying a shear strain at a constant rate of 10^7 s^{-1}, up to a total strain of 2.5% at 900 K. The loops were found to be stable and did not unfault up to the maximum strain, corresponding to a shear stress of 1.3 GPa. The configurations of loops, visualized using central symmetry analysis [38], at the beginning and at the end of load are shown in figure 8. We see that the extrinsic stacking fault was not removed under load, although the imposed shear stress caused the splitting of 1/3 ⟨1 1 1⟩ dislocation segments aligned along the ⟨1 1 0⟩ directions (see configurations *d* and *e* in figure 8) in 'cir_FL' and '1 1 0_FL', thus forming stair rod dislocations and additional faults

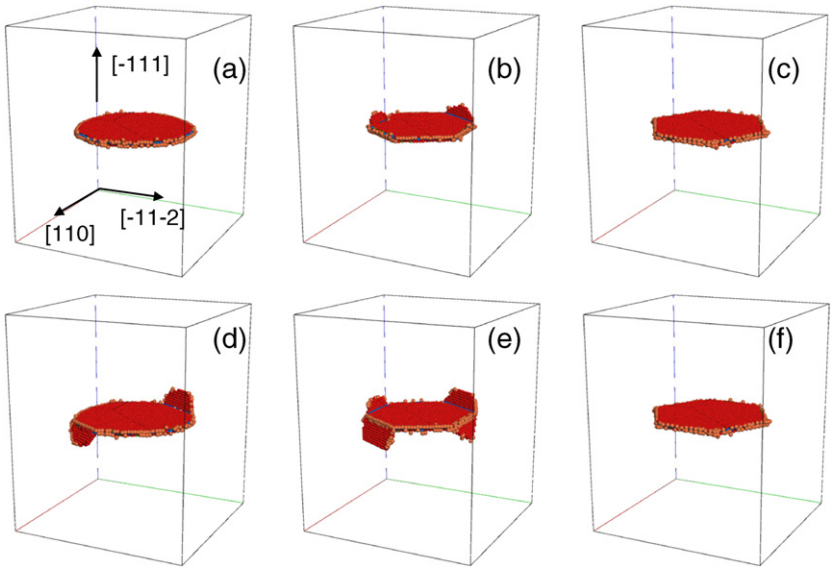

Figure 8. Frank loops (a =cir_FL, b =1 1 0_FL and c =1 1 2_FL) of interstitial type thermalized at 900 K before (upper row) and after (lower row) load. Details regarding the loading conditions are found in the text.

in the inclined $\{1\,1\,1\}$ planes. We attribute this effect to the stress, because no such splitting has been observed in the circular loop under thermal annealing. We can therefore conclude that Frank loops of size 10 nm and below are stable under a shear stress of ∼1 GPa in the temperature range 0–900 K in the target composition alloy.

4. Summary and conclusions

We have developed an EAM type interatomic potential for the ternary FeNiCr system to model movement of dislocations and their interaction with radiation defects. Special attention has been drawn to the Fe–10Ni–20Cr alloy, whose properties were ensured to be close to those of 316L austenitic stainless steels. In particular, the SFE and elastic constants are well reproduced.

Given the good reproduction of the latter properties, preliminary simulations were run to test the suitability of the potential for plasticity studies. Based on the zero Kelvin elastic constants (C' in particular) the stability of the fcc phase against small deformations and temperature was confirmed. In addition, the fcc phase for the Fe–10Ni–20Cr random alloy was proven to be stable in the temperature range 0–900 K and under shear strain up to 5%.

Then, the glide of screw dislocations and stability of Frank loops in the target alloy was checked. The glide of a $1/2\langle 1\,1\,0\rangle\{1\,1\,1\}$ screw dislocation in the Fe–10Ni–20Cr alloy was modelled at 300 K using a periodic array of dislocations under constant strain rate conditions. The dislocation was found to split into two partials connected by a stacking fault ribbon of ∼10 nm width. During the MD runs, no constriction of the ribbon nor dislocation cross slip was observed. The Frank loops of different shapes and sizes (up to 10 nm) were also found to be stable at finite temperature under substantial load. These results suggest that the developed potential is suitable to study the movement of dislocations and their interaction with Frank loops in an alloy with properties close to 316L austenitic steels.

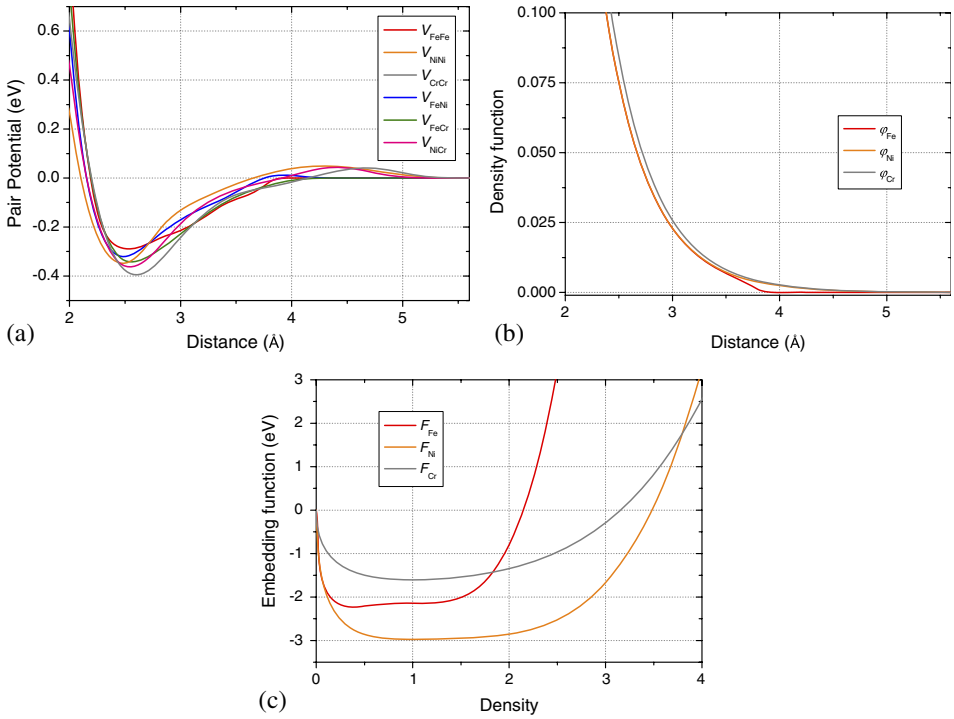

Figure A.1. Plot of the potential functions: pair potentials (*a*), density functions (*b*) and embedding functions (*c*).

Acknowledgments

This work was performed in the framework of the EC-funded FP7/PERFORM60 project, under grant agreement 232612. The work was also partially sponsored by the Belgo-Argentine FWO-MINCYT bilateral cooperation agreement, Project VS.004.10N. Part of the calculations were performed on the HPC cluster Jülich within the APM project. AB acknowledges financial support from FWO-Vlaanderen.

Appendix

The optimized parameter sets used in equations (3)–(5) are summarized in table A.1. A visualization of the potential functions (in effective gauge [11]) is given in figure A.1. These figures illustrate that the potential functions are smooth and that no significant oscillations occur.

Table A.1. Summary of the potential parameters. The energy and distance units are eV and Å, respectively.

k	r_k	a_k		
FeFe				
1	2.5	2.660 526	$A = -8.666\,245\,13$	$r_{cut} = 4.0$
2	2.8	3.566 762 07	$B = 9.413\,754\,92$	$\beta = 2.0$
3	3.1	−1.272 9965	$C = -3.237\,213\,54$	$h = 0.25$
4	3.4	2.100 276 86	$D = 0.348\,448\,677$	$S = 27.868\,9586$
5	3.7	−0.901 005 963		$K = 18.827\,5098$
6	4.0	0.393 902 864		

Table A.1. Continued

k	r_k	a_k		
7	2.4	12.0		
8	2.0	100.0		
NiNi				
1	2.5	−1.813 934 25	$A = -7.865\,656\,25$	$r_{\text{cut}} = 5.6$
2	2.844 444 44	4.303 289 23	$B = 5.951\,077\,74$	$\beta = 2.0$
3	3.188 888 89	−0.425 690 56	$C = -1.110\,141\,59$	$h = 0.25$
4	3.533 333 33	0.156 449 935	$D = 0.050\,508\,392$	$S = 27.875\,0306$
5	3.877 777 78	0.035 027 069		$K = 11.902\,1555$
6	4.222 222 22	0.149 366 37		
7	4.566 666 67	0.010 832 29		
8	4.911 111 11	−0.019 697 11		
9	5.255 555 56	−0.137 669 014		
10	5.6	0.085 392 233		
11	2.4	4.5		
12	2.0	100.0		
CrCr				
1	2.5	1.731 704 02	$A = -3.625\,808\,68$	$r_{\text{cut}} = 5.6$
2	2.942 857 14	1.841 434 06	$B = 2.266\,361\,49$	$\beta = 2.0$
3	3.385 714 29	0.755 016 121	$C = -0.265\,780\,601$	$h = 0.25$
4	3.828 571 43	−0.468 318 806	$D = 0.019\,526\,015$	$S = 31.261\,3817$
5	4.271 428 57	−0.047 416 719		$K = 4.532\,722\,97$
6	4.714 285 71	0.461 509 957		
7	5.157 142 86	−0.410 733 637		
8	5.6	0.113 373 503		
9	2.0	100.0		
FeNi				
1	2.0	62.418 0774	$K = 0.0$	
2	2.357 142 86	4.442 735 75		
3	2.714 285 71	2.402 634 93		
4	3.071 428 57	0.627 280 711		
5	3.428 571 43	−1.153 962 15		
6	3.785 714 29	1.318 395 61		
7	4.142 857 14	−0.707 8573		
8	4.5	0.099 942 305		
FeCr				
1	2.0	62.393 2019	$K = 0.0$	
2	2.342 857 14	4.649 491 19		
3	2.685 714 29	2.410 933 47		
4	3.028 571 43	0.101 143 751		
5	3.371 428 57	0.439 673 171		
6	3.714 285 71	−0.239 918 132		
7	4.057 142 86	0.218 918 034		
8	4.4	−0.153 852 387		
NiCr				
1	2.0	71.465 182	$K = 0.0$	
2	2.478 571 43	0.686 470 816		
3	2.957 142 86	1.799 965 78		
4	3.435 714 29	0.044 759 399		
5	3.914 285 71	−0.470 971 247		
6	4.392 857 14	0.585 425 288		
7	4.871 428 57	−0.417 474 26		
8	5.35	0.102 0253		

References

[1] Roberts J T A 1981 *Structural Materials in Nuclear Power System* (New York: Plenum)
[2] Ma B M 1983 *Nuclear Reactor Materials and Applications* (Princeton, NJ: Van Nostrand-Reinhold)
[3] Leclercq S, Lidbury D, Van Dyck S, Moinereau D, Alamo A and Al Mazouzi A 2010 *J. Nucl. Mater.* **406** 193
[4] Daw M S and Baskes M I 1984 *Phys. Rev.* B **29** 6443
[5] Grujicic M and Zhou X W 1993 *CALPHAD* **17** 383
[6] Smith R W and Was G S 1989 *Phys. Rev.* B **40** 10322
[7] Bonny G, Pasianot R C and Malerba L 2009 *Modelling Simul. Mater. Sci. Eng.* **17** 025010
[8] Malerba L *et al* 2010 *J. Nucl. Mater.* **406** 7
[9] Olsson P, Wallenius J, Domain C, Nordlund K and Malerba L 2005 *Phys. Rev.* B **72** 214119
[10] Bonny G, Pasianot R C, Terentyev D and Malerba L 2011 *Phil. Mag.* **91** 1724
[11] Müller M, Erhart P and Albe K 2007 *J. Phys.: Condens. Matter.* **19** 326220
[12] Finnis M W and Sinclair J E 1984 *Phil. Mag.* A **50** 45
[13] Ercolessi F, Parrinello M and Tosatti E 1988 *Phil. Mag.* A **58** 213
[14] Johnson R A 1989 *Phys. Rev.* B **39** 12554
[15] Bonny G and Pasianot R C 2010 *Phil. Mag. Lett.* **90** 559
[16] Kittel C 1996 *Introduction to Solid State Physics* (New York: Wiley)
[17] Rose J H, Smith J R, Guinea F and Ferrante J 1984 *Phys. Rev.* B **29** 2963
[18] Ehrhart P 1991 *Atomic Defects in Metals* (New York: Springer) p 88
[19] Mishin Y, Mehl M J and Papaconstantopoulos D A 2005 *Acta Mater.* **53** 4029
[20] Tucker J D, Najafabadi R, Allen T R and Morgan D 2010 *J. Nucl. Mater.* **405** 216
[21] Klaver T P C, Ackland G J and Hepburn D J 2011 The effect of magnetic ordering on defect and solute properties in dilute FeNiCr austenitic steels *Phys. Rev.* B submitted (arXiv:1107.0260)
[22] Olsson P and Domain C 2011 private communication
[23] Simmons G and Wang H 1977 *Single Crystal Elastic Constants and Calculated Aggregate Properties* (Cambridge, MA: MIT Press)
[24] Murr L E 1975 *Interfacial Phenomena in Metals and Alloys* (Reading, MA: Addison-Wesley)
[25] Miodownik A P 1978 *CALPHAD* **2** 207
[26] Denteneer P J H and van Haeringen W 1987 *J. Phys. C: Solid State Phys.* **20** L883
[27] Goodchild D, Roberts W T and Wilson D V 1970 *Acta Metall.* **18** 1137
[28] Kelly A and Groves G W 1970 *Crystallography and Crystal Defects* ed J D Arrowsmith (Harlow: Longmans) p 255 chapter 8
[29] Hertzberg R W 1989 *Deformation and Fracture Mechanics of Engineering Materials* 3rd edn (New York: Wiley) p 67
[30] Silk M G, Lidington B H and Hammond G F 1980 *Br. J. Non-Destr. Test.* **22** 55
[31] Ledbetter H M 1981 *Br. J. Non-Destr. Test.* **34** 286
[32] Ledbetter H M 1985 *Ultrasonics* **23** 9
[33] Osetsky Y N and Bacon D J 2003 *Modelling Simul. Mater. Sci. Eng.* **11** 427
[34] Zinkle S J, Maziasz P J and Stoller R E 1993 *J. Nucl. Mater.* **206** 266
[35] Lee E H, Hunn J D, Hashimoto N and Mansur L K 2000 *J. Nucl. Mater. Mater.* **278** 266
[36] Pokor C, Brechet Y, Dubuisson P, Massoud J-P and Barbu A 2004 *J. Nucl. Mater.* **326** 19
[37] Kadoyoshi T, Kaburaki H, Shimizu F, Kimizuka H, Jitsukawa S and Li J 2007 *Acta Mater.* **55** 3073
[38] Rodney D 2004 *Acta Mater.* **52** 607